Composites Part B 250 (2023) 110433

Contents lists available at ScienceDirect

Composites Part B

journal homepage: www.elsevier.com/locate/compositesb

Fracture performance of fibre-reinforced epoxy foam

George Irven [a,b], Declan Carolan [a,b,*], Alexander Fergusson [a,b], John P. Dear [b]

[a] FAC Technology, 53 Lydden Grove, London, SW18 4LW, UK
[b] Department of Mechanical Engineering, Imperial College London, London, SW7 2AZ, UK

ARTICLE INFO

Keywords:
Epoxy foam
Fracture toughness
Fibre-reinforced
Fractography

ABSTRACT

Low density aramid and carbon fibre-reinforced epoxy foam has been synthesised with the aim of improving mechanical properties, principally fracture performance. The foam properties measured were fracture energy, compressive strength, and density. The influence of fibre type, loading, and length was investigated. In addition, composite face-sheet bond tests were performed to ascertain how effective toughness transferred from individual component to composite structure. In general, the addition of fibres improved the mechanical performance of reinforced samples compared to the control foam. Increases in compressive strength were moderate whilst fracture energy was increased by up to 107% from 124 J/m^2 to 256 J/m^2 by the addition of 0.75 mm aramid fibres. Increased fracture energy of the foam and the presence of fibres on the foam surface, caused an increase in face-sheet bond propagation fracture toughness of 50% from 277 J/m^2 to 416 J/m^2.

1. Introduction

The combination of high specific strength, corrosion resistance and low radar signature makes composite sandwich structures an attractive structural choice for many disciplines [1]. However, the brittle nature of composite materials can lead to substantial overdesign of sandwich structure components, counteracting their weight and cost savings benefits. The toughness of a composite sandwich structure, which is a critical parameter for it to withstand damage, can be improved by improving the toughness of the individual components. Previous research by this group has demonstrated that by altering the layup of the individual plies in the composite face-sheets, a significant increase in impact resistance of the structure can be obtained [2]. More recently, impact performance of sandwich structures has been improved through toughening the matrix of the sandwich face-sheet [3]. During the impact testing of the epoxy-foam-core sandwich structures in the previous research, extensive cracking within the core was found. As such, this project builds on this research further and details a systematic study of the effect of reinforcing epoxy foam with short-cut carbon and aramid fibres with the aim of increasing strength and toughness. Toughness is a crucial property for foams as in tension they fail by the propagation of a single crack [4]. Marsavina and Linul [5] recently conducted a comprehensive review of the fracture toughness of polymer foams including reinforcement methods.

Reinforcement of epoxy foam has experienced attention from a variety of researchers in recent years, Song et al. [6] produced short carbon fibre-reinforced epoxy foams via mechanical frothing and achieved an increase in toughness of up to 113% at densities ranging from 362 to 475 kg/m^3. Alonso et al. [7] synthesised short fibre-reinforced epoxy foam with both glass and aramid fibres at a density of 300 kg/m^3. Improvements in shear and compressive strength were substantial, especially in the foam rise direction. Alonso et al. highlight the importance of using a suitable coupling agent between fibre and matrix to ensure effective strengthening. They also worked on modelling of the compressive properties of glass fibre-reinforced epoxy foam using a statistical approach [8]. The foams ranged from 250 to 550 kg/m^3 and the variables that were studied were density, fibre weight fraction, and fibre length. They note that more variables such as fibre aspect ratio and stiffness could be included for increased accuracy.

Fibre modification of polymer foams has been the subject of research for some time. Cotgreave and Shortall [9–11] investigated polyurethane foams reinforced with chopped glass fibres. Increases in tensile strength were moderate, up to 22%, while increases in toughness were more pronounced, up to 45%. Fibres were found to lie within struts and shown to arrest or deflect cracks propagating through the foam matrix causing fibre pull-out to occur. They found that individual filaments well distributed within the foam were more effective than fibre bundles. Carling [12] tested polyurethane foams reinforced with 7 mm glass fibres at a density of 80 kg/m^3 Limited gains in fracture energy were realised, however, modulus and critical stress intensity factor were

* Corresponding author. FAC Technology, 53 Lydden Grove, London, SW18 4LW, UK.
E-mail address: d.carolan@imperial.ac.uk (D. Carolan).

https://doi.org/10.1016/j.compositesb.2022.110433
Received 28 March 2022; Received in revised form 9 October 2022; Accepted 17 November 2022
Available online 18 November 2022

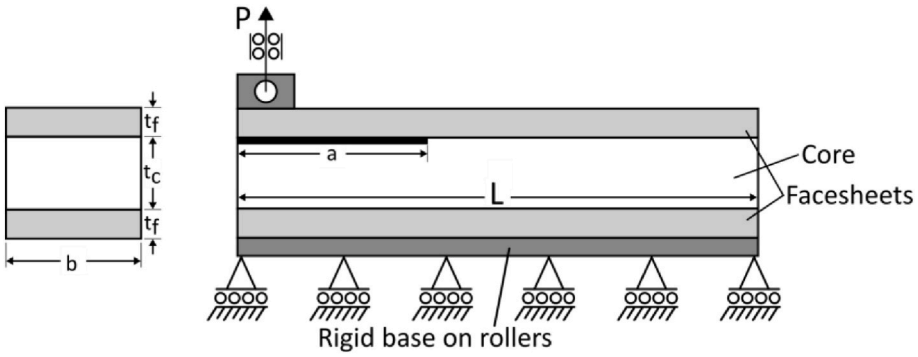

Fig. 1. SCB schematic.

improved. It was noted that improvements in mechanical performance were limited due to the fibres being bundled together as opposed to being individually distributed throughout the foam. Significant work has been carried out on fibre-reinforced phenolic foams [13–16], improvements in compressive, tensile, shear, and friability properties were substantial.

The failure mode of face-core debonding can cause significant decreases in the structural integrity of sandwich panels as it prevents shear transfer between face sheets [17]. Recent single cantilever beam (SCB) tests by Irven et al. [3] found that systematically modifying the matrix resin of the sandwich face-sheet caused a change in failure mode at the face-core interface. When the matrix resin has high strength, the failure mode involves significant foam fracture whereby portions of foam remain on the face after testing. As such, it was expected that an improvement in foam fracture performance caused by the addition of short fibres would translate to an improvement in SCB interface toughness. Furthermore, Shen et al. [16] reported a seven-fold increase in peel resistance with the addition of 3 wt percentage (wt%) 6.4 mm aramid fibres in phenolic foam.

The current research investigates reinforced epoxy foams at a nominal density of 170 kg/m^3 with the aim of improving the mechanical properties of the epoxy foam. A key aim of this work was to maintain a low density for all reinforced foams to maximise utility in real-world applications. Previous research in the literature has mainly focussed on high density epoxy foams [6,7].

2. Materials

A commercially sensitive epoxy based foaming resin formed the basis of the materials investigated in the current work. The nominal density of the cured foam in the current work is 170 kg/m^3. Short-cut para-aramid and carbon fibres were sourced from Barnet Europe. Aramid fibres had cut lengths of 0.75 mm, 3 mm, and 6 mm and an average diameter of 12 μm. Carbon fibres had cut lengths of 1.5 mm, 3 mm, and 6 mm and an average diameter of 8 μm. Manufacturing limitations prevented 0.75 mm carbon fibres being cut. Both short-cut fibre types were appropriately sized for use with epoxy. Milled carbon fibres were sourced from ELG Carbon Fibre with average length 0.6 mm and an average diameter of 7 μm. The milled fibres used were unsized prior to milling and were used as received.

Reinforced epoxy foams were synthesised via a dispersing homogenising blade attached to a mounted mixer with a maximum rotational speed of 2800 rpm to disperse fibres in the foaming resin. High-speed mixing took place with a resin temperature of 70 °C to minimise viscosity and ensure the good dispersion of the various fibres. A stoichiometric amount of a commercially sensitive amine-based hardener was then added, these constituents were then mixed thoroughly again. The mixture was noted to begin foaming shortly after mixing and was poured into a rectangular mould and cured at 21 °C for 24 h, followed by a 24 h post-cure at 40 °C. The long cure cycle at a precisely controlled temperature is required when manufacturing foams as the viscosity, particularly the thixotropic response, of the foam is critical to developing and maintaining an optimal microstructure at a target density. The fibre loadings used in parts per hundred resin (PHR) were 0.5, 1, 2.5, and 5. For 3 mm and 6 mm fibres, it was only possible to load the resin with 0.5 and 1 PHR, higher loading caused a drastic increase in viscosity and resulted in a poor-quality foam.

Carbon fibre-reinforced polymer (CFRP) composite sandwich panels were manufactured for single cantilever beam (SCB) testing. The carbon fibre used was 385 gsm of H2550 fibres in 12 k tows in a 0/90 non-crimp fabric, the SCB sandwich panels used $[[0/90]4]_s$ for 8 plies in each face-sheet. An amine-cured epoxy system formed the matrix of the SCB panels. The resin was a standard diglycidyl ether of bisphenol-A (DGEBA) with an epoxide equivalent weight of 185 g/eq. This was cured with a stoichiometric amount of a difunctional primary amine (JEFFAMINE D-230) from Huntsman, UK. The composite sandwich panels were laid up on a flat release-coated aluminium plate and sealed using a vacuum bag. The infusion then took place over a period of 5–10 min and was then cured under vacuum for 10 h at 40 °C and 10 h at 55 °C.

3. Methods

Single-edge notched bending (SENB) tests in three-point bend configuration were conducted to determine the fracture energy, G_c, in accordance with ASTM D-5045 [18]. Multiple studies have confirmed the SENB specimen to be suitable for fracture toughness testing in foam [19,20]. In order to satisfy the plane strain condition, test specimens were machined with dimensions 140 mm × 28 mm × 14 mm. These specimens were notched to a depth of 14 mm with a razor blade held in a custom device that was fixed to a drill press, allowing a consistent notch depth to be achieved. Razor blades are frequently used in the literature to create cracks in foam fracture toughness specimens [11,12,17,21,22]. All mechanical testing was conducted using an 'Instron 4466' screw-driven universal testing machine fitted with a 10 kN load cell. The SENB specimens were tested at a constant crosshead displacement rate of 1 mm/min. The fracture energy, G_{Ic} was calculated using the energy method via:

$$G_{Ic}(\text{bulk}) = \frac{U}{bw\varphi} \tag{1}$$

Where U is the energy under the corrected load-displacement curve and φ is an energy calibration factor as defined in the ASTM standard (b and w are the breadth and width of the sample respectively) [18]. At least five replicate specimens were tested for each formulation.

The compressive properties of the epoxy foam were tested according to ASTM D1621 [23] using a screw-driven universal testing machine. Samples with dimensions of 30 × 30 × 30 mm^3 cubes were cut from foam panels with a diamond saw. The samples were placed between stainless steel testing platens, and a load was then applied with a

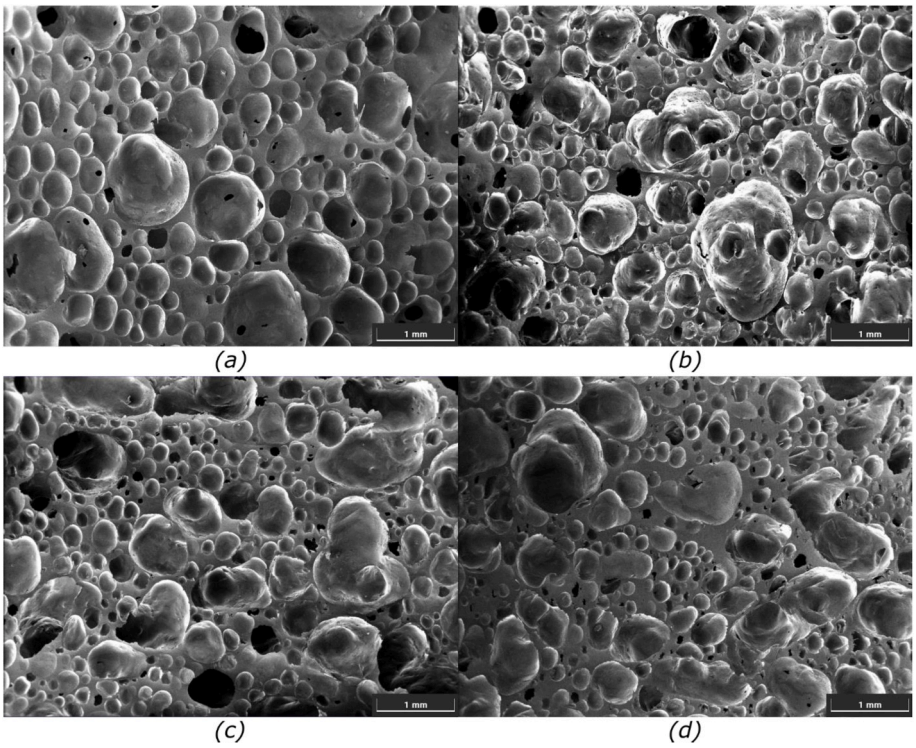

Fig. 2. SEM images of polished aramid foam samples. (a): Control (b): 0.75 mm 2.5 PHR (c): 3 mm 0.5 PHR. (d): 6 mm 1 PHR.

crosshead rate of 2 mm/min. Compressive strength was calculated from the maximum stress within a strain of 10%. The compression samples were also used to calculate density. The samples were measured and weighed with an electronic balance. Measuring multiple samples allowed for variations in density across a foam panel to be monitored.

Imaging of both polished and fractured foam samples was conducted using a Tescan Mira scanning electron microscope (SEM). Polished samples were prepared using a standard wet grinding technique up to 2000 grit sandpaper. Imaging of the polished samples revealed valuable information regarding the morphology and microstructure of the foams. A tight distribution of void size is typically a good indicator of subsequent good mechanical performance. Additional images of the fractured samples were also taken with a high-resolution digital camera. The camera used was a Canon EOS 5DS R with a 100 mm macro lens.

Many test methods have been developed to test mode I debonding of a sandwich skin, they are summarised by Ratcliffe [24,25] who also developed a test using a lengthened loading arm in an attempt to standardise the test. However, the focus here will be on the SCB test as used by Glaessgen et al. [26] illustrated in Fig. 1. This method allows an apparent mode I critical strain energy release rate to be measured most accurately as discussed by Ratcliffe [24] and Adams [27,28]. Ratcliffe also carried out a sizing study which proposes an algorithm, based on limitations of the material used, to determine appropriate dimensions for SCB specimens [24,25]. Dimension limitations such as sizing the initial debond length to ensure bending is the dominant deformation mode of the loaded face sheet are outlined in a step-by-step manner. This sizing system has been followed for the material properties of the sandwich structures in the current research. There are difficulties to measuring pure mode-I fracture properties of an interface between dissimilar materials; indeed, the measured mode is often mixed [29]. The difference of elastic properties between, in this instance, the skin and core, will disrupt the symmetry even if the geometry and loading are symmetric. The mismatch in modulus will couple the normal and shear deformations ahead of the debond front [24]. Consequently, the measured critical strain energy release rate will not be referred to as mode-I, G_{Ic}, but G_c and should be considered as a fracture energy that is mode-I dominant but not pure mode-I. It should be noted that it is expected that the mode-mixity for the SCB test used in this research is minimal. Adams et al. [27,28] conducted finite element analyses to evaluate the mode-mixity of various face-sheet debonding test methods. They found that the SCB test method was the most appropriate for minimising bending stresses in the core, eliminating crack kinking, and minimising any mode-II component at the crack tip to below 5%. In fact, they found that the mode-I component is over 98% for the sandwich configurations evaluated.

SCB tests were conducted with both the control foam and the 2.5 PHR 0.75 mm Aramid fibre foam. Test specimens of 25 mm × 185 mm were cut from a panel with a core thickness of 10 mm and a face-sheet thickness of 3.2 mm. A 12 μm thick PTFE crack starter film of length 55 mm was used to ensure an appropriately sharp starter crack. The corrected beam theory (CBT) method was employed to calculate both the initiation fracture energy, $G_{c,init}$, and the steady-state propagation fracture energy, $G_{c,prop}$, of the composites. Each specimen is clamped to a roller that is free to move on a track perpendicular to the crosshead direction but is otherwise built-in. The tests were conducted at a constant crosshead displacement rate of 2 mm/min using a screw-driven tensile testing machine. The loads and displacements were recorded, and the crack lengths monitored using a high-resolution digital camera setup for magnification and periodic imaging. At least five replicate specimens were tested for each foam used.

4. Results

4.1. Microscopy: polished aramid-reinforced foam

Each foam sample was cut and polished to give a smooth surface to image using an SEM. An SEM image of one foam containing each aramid fibre length is shown in Fig. 2. The images show cells surrounded by nodes connected by cell walls. The images show the foams have bimodal cell size distributions with many small cells surrounding fewer larger cells. The cell sizes do not appear to change significantly across the aramid fibre-reinforced formulations. However, the small cells in the

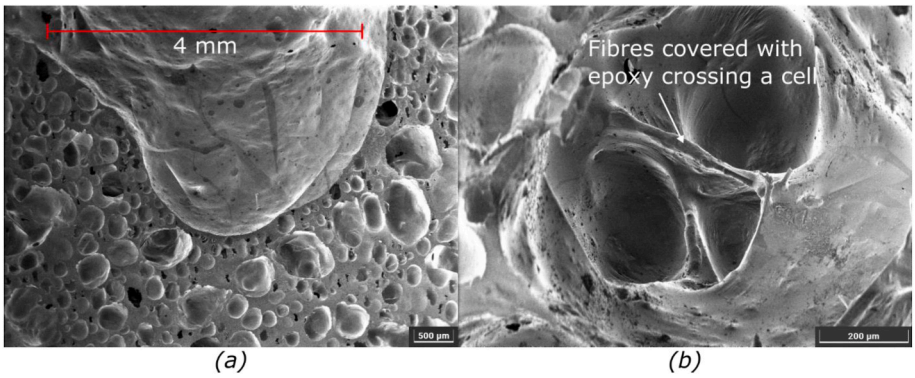

Fig. 3. SEM images of polished aramid foam samples. (a): Large void in 6 mm 1 PHR. (b): Epoxy covered fibres in 0.75 mm 2.5 PHR.

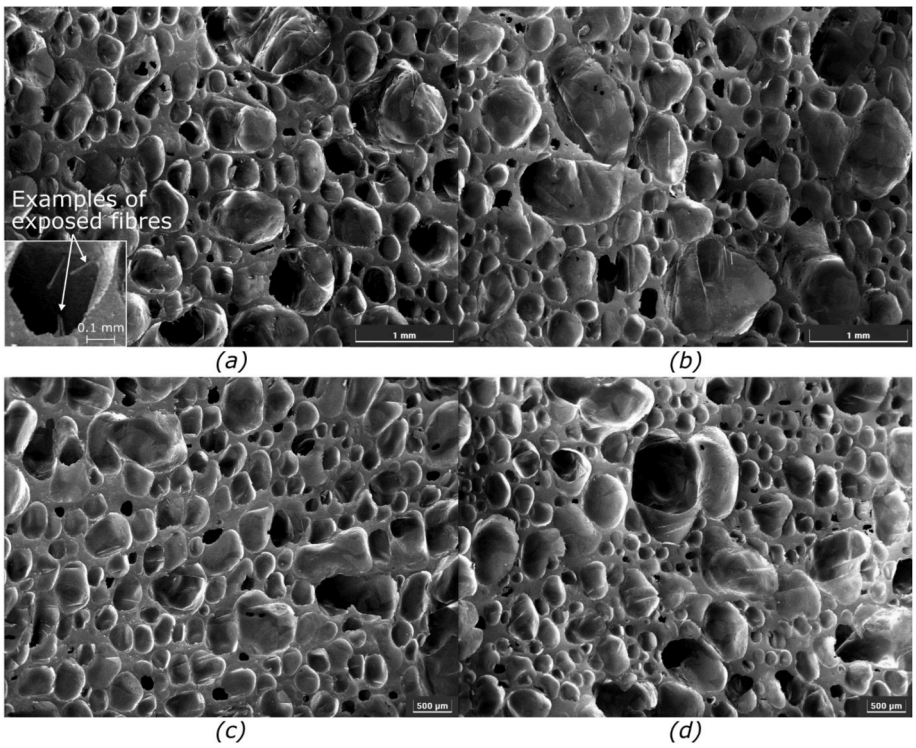

Fig. 4. SEM images of polished carbon foam samples. (a): Milled fibre 2.5 PHR. (b): 1.5 mm 1 PHR. (c): 3 mm 1 PHR. (d): 6 mm 1 PHR.

aramid fibre-reinforced foams appear somewhat smaller than in the control foam. The images also show that there is a slight loss of sphericity in the cells between Fig. 2 (a) and Fig. 2 (b), (c), and (d). In the 3 mm and 6 mm aramid foams, very large voids could be found. This is shown clearly in Fig. 3 (a). These voids could measure up to 6 mm across and were difficult to get an entire void within the field of view of the microscope. Large voids in fibre-reinforced foam with fibres of similar length have been previously reported in the literature [6,12].

During the manufacturing process of the foam, all fibres are completely wetted with liquid epoxy. Furthermore, the aramid fibres are sized appropriately for use in epoxy. As a result, the fibres in the finished foam are covered in epoxy. This is the case even if the fibres do not

Table 1
Measured properties of aramid reinforced foam.

Fibre Length [mm]	Fibre Loading [PHR]	*Fracture Energy* G_{Ic} [J/m^2]	% change	Compressive Yield Strength [MPa]	% change	Density [kg/m^3]	% change	Compressive Modulus [MPa]
–	–	124 ± 13	00	2.33 ± 0.03	00	175.1 ± 0.8	00	86.5 ± 4.9
0.75	0.5	113 ± 14	−08	2.46 ± 0.01	+06	187.8 ± 0.8	+07	81.3 ± 2.5
	1	137 ± 25	+11	2.52 ± 0.05	+08	191.7 ± 1.4	+09	98.3 ± 2.3
	2.5	208 ± 45	+68	2.56 ± 0.06	+10	199.6 ± 5.7	+14	99.0 ± 4.8
	5	256 ± 30	+107	2.28 ± 0.04	- 02	200.1 ± 0.6	+14	89.9 ± 1.7
3	0.5	133 ± 23	+07	2.46 ± 0.02	+06	189.8 ± 1.5	+08	94.3 ± 2.8
	1	165 ± 28	+33	2.44 ± 0.07	+05	194.0 ± 1.1	+11	95.5 ± 0.8
6	0.5	143 ± 31	+16	2.33 ± 0.09	00	190.6 ± 5.1	+09	88.4 ± 6.3
	1	204 ± 44	+65	2.43 ± 0.05	+04	203.3 ± 3.5	+16	94.2 ± 4.3

Table 2
Measured properties of carbon reinforced foam.

Fibre Length [mm]	Fibre Loading [PHR]	*Fracture Energy* G_{Ic} [J/m^2]	% change	Compressive Yield Strength [MPa]	% change	Density [kg/m^3]	% change	Compressive Modulus [MPa]
–	–	124 ± 13	00	2.33 ± 0.03	00	175.1 ± 0.8	00	86.5 ± 4.9
0.6	0.5	161 ± 37	+30	2.48 ± 0.02	+07	175.4 ± 0.4	00	84.9 ± 2.9
	1	168 ± 40	+36	2.55 ± 0.03	+10	176.2 ± 1.0	+01	92.6 ± 1.6
	2.5	180 ± 33	+45	2.58 ± 0.04	+11	178.4 ± 0.8	+02	91.9 ± 3.2
	5	245 ± 59	+98	2.38 ± 0.09	+02	184.5 ± 0.9	+05	93.3 ± 5.3
1.5	0.5	140 ± 26	+13	2.41 ± 0.03	+04	176.5 ± 0.2	+01	89.7 ± 2.3
	1	157 ± 33	+27	2.48 ± 0.05	+06	177.7 ± 0.5	+01	95.8 ± 2.6
3	0.5	137 ± 16	+10	2.15 ± 0.05	- 08	172.5 ± 0.6	- 01	69.3 ± 1.2
	1	201 ± 13	+62	1.87 ± 0.05	- 20	173.6 ± 1.2	- 01	65.2 ± 0.9
6	0.5	159 ± 57	+29	1.93 ± 0.04	- 17	172.3 ± 1.4	- 02	69.0 ± 4.1
	1	187 ± 43	+51	1.83 ± 0.01	- 21	176.7 ± 0.9	+01	74.3 ± 3.8

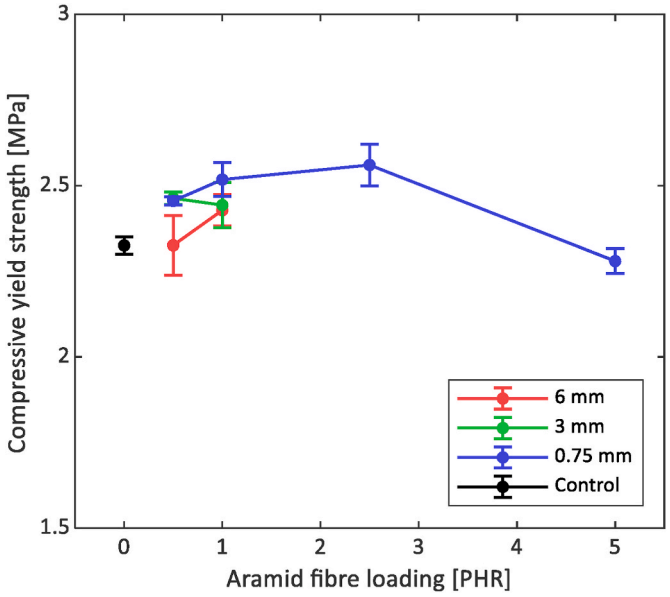

Fig. 5. Compressive yield versus fibre loading for aramid fibre-reinforced foams.

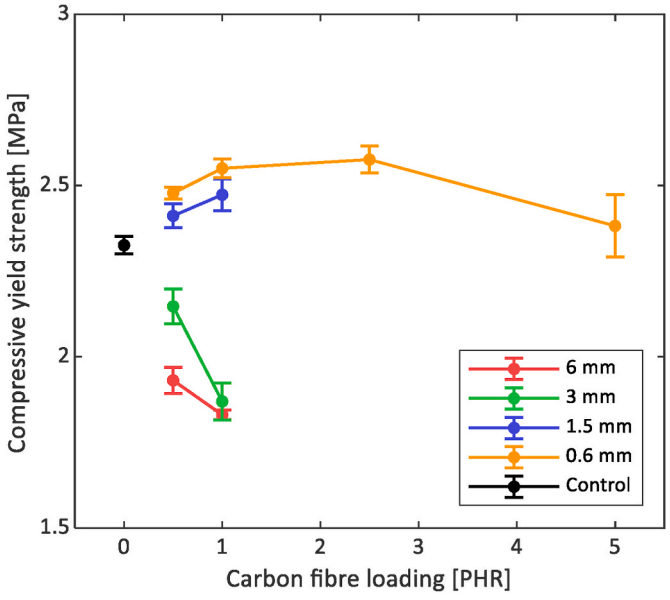

Fig. 6. Compressive yield versus fibre loading for carbon fibre-reinforced foams.

completely lie within a natural cell wall, epoxy will encapsulate the fibre and bridge to the cell wall, an example of this is shown in Fig. 3 (b). Exposed fibres, with no epoxy sheath, are very rare within the polished samples.

4.2. Microscopy: polished carbon-reinforced foam

Fig. 4 shows polished samples of foams containing each carbon fibre length. Again, there is a slight loss of spheroidicity in the cells between the control foam in Fig. 2 (a) and the four foams in Fig. 4. However, there appears to be less of a bi-modal distribution of cell sizes within the carbon-reinforced foams. As with the aramid foams, the 3 and 6 mm foams have some large voids which were avoided for these SEM images as the voids could measure up to 6 mm across. Similar to the chopped aramid fibre foams, the chopped carbon foams do not show exposed fibres when polished. However, some exposed fibres can be seen in the milled carbon fibre foam in Fig. 4 (a), this is related to the lack of sizing on the milled carbon fibres.

4.3. Compression

The compressive yield strengths of the aramid and carbon fibre-reinforced foams are presented in Table 1 and Table 2, and are plotted in Figs. 5 and 6 respectively. The compressive yield strength of the foam is increased by up to 10% by adding fibres. All aramid fibre lengths give rise to an increase in compressive strength, however, adding 5 PHR 0.75 mm aramid fibre causes the compressive yield to drop below that of the control. A similar trend is observed when adding 0.6 and 1.5 mm carbon fibres, 5 PHR 0.6 mm causes strength to drop back to that of the control. It is clear that, to maximise compressive yield, approximately 2.5 PHR of the shortest fibre length is optimal for both fibre types. While short carbon fibres improve compressive yield, the 3 and 6 mm carbon fibres reduce the yield strength of the foam. A visual inspection reveals the 3 and 6 mm carbon fibre-reinforced foams have some large voids such as the one in Fig. 3. These large voids cause a drop in yield strength by reducing the total load bearing area of a foam sample. In contrast, short fibres do not reduce the quality of the foam in the same way. While the long aramid fibre-reinforced foams also display large voids, the increase in density of these foams prevents a potential drop in yield strength. The compressive modulus values of the aramid and carbon fibre-reinforced foams are also presented in Tables 1 and 2. These values follow the same trends as the compressive strength values. However, the standard deviations of the modulus values are larger than the standard deviations of the strength values. There are significant difficulties with accurately measuring strain in a compressive test of structural foam as discussed in detail by Rajput et al. [30]. Primarily, parts of the sample can begin to fail and form a crush band, as a result, the strain throughout the sample can vary massively. Furthermore, when a foam sample is machined, the top and bottom layer of cells are broken and are therefore very compliant. Consequently, the measured modulus will both be lower than the true modulus and it will be sample size dependent.

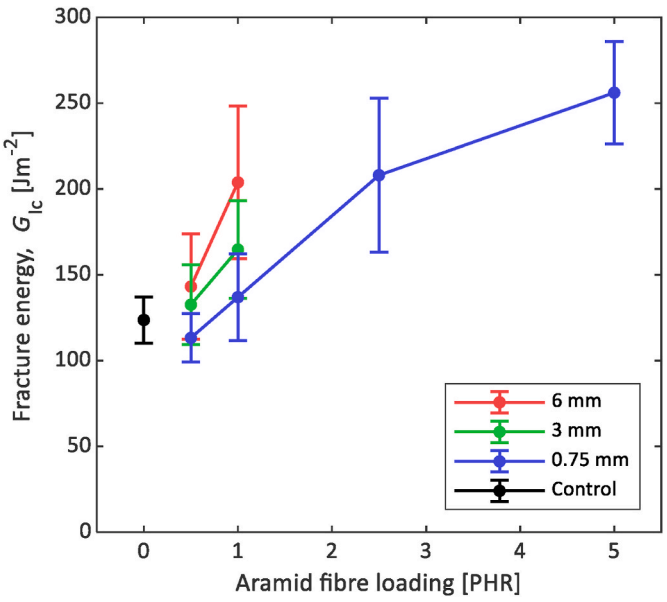

Fig. 7. Fracture energy versus fibre loading for Aramid fibres.

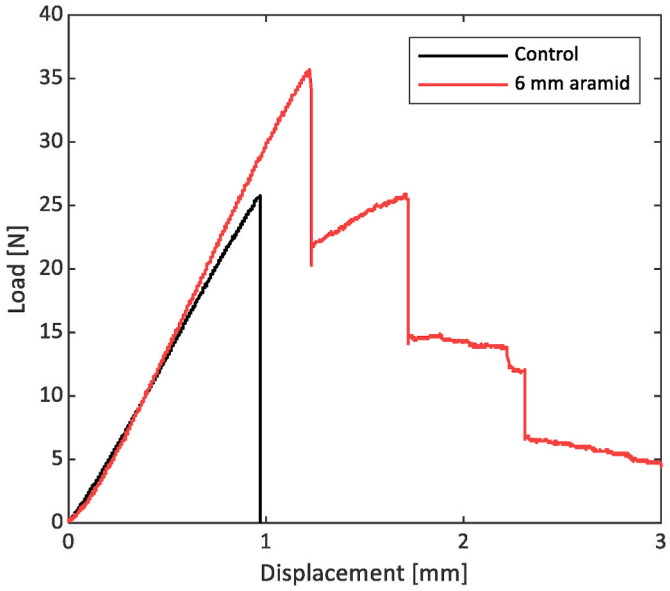

Fig. 8. Load-displacement curves for the SENB testing of aramid 6 mm and control.

4.4. Density

It is interesting to note the effect on density associated with each fibre type, length, and loading. The density of aramid and carbon fibre-reinforced foam can be found in Tables 1 and 2 respectively. The addition of carbon fibres does little to increase the density of the foam, clearly a benefit in any potential application. However, the addition of aramid fibres moderately increases the density of the foam. The addition of 5 PHR 0.75 mm aramid fibre produces a foam of 200 kg/m^3, 14% denser than the control. However, this increase in density is far outweighed by the 107% increase in fracture energy. Furthermore, longer aramid fibres have an increased effect on the density with 1 PHR 6 mm producing a foam with a density of 203 kg/m^3. The increase in density is partially caused by the addition of the denser fibres. Both aramid and carbon fibres are denser than the epoxy polymer. The density is primarily affected by the inhibiting effect the fibres have on the foaming process due to the increased viscosity of the fibre resin mixture. It can be inferred that carbon fibres impede the foaming process significantly less than aramid fibres. In fact, the large voids in the 3 and 6 mm carbon fibre-reinforced foams have caused the overall density to be lower than the control. In these foams, the longer fibres have a tendency to mat together forming a barrier in the resin and effectively trap more gas during the foaming process than the resin would otherwise, forming large voids in the process.

4.5. Fracture properties

4.5.1. Fracture energy: Aramid-Reinforced Foam

Fracture energies for all the manufactured aramid fibre-reinforced foams are given in Table 1, all data shows the calculated average, standard deviation, and percentage difference to the control. The fracture energy, G_{Ic}, versus fibre loading of each of the aramid reinforced foams is shown in Fig. 7. The addition of aramid fibres was found to greatly increase the toughness of the foam from 124 J/m^2 to a maximum of 256 J/m^2. It is clear that, for a similar fibre loading, longer fibres induce a greater increase in toughness in the foam. For example, a loading of 1 PHR 6 mm aramid fibres produces a similar toughness to a loading of 2.5 PHR 0.75 mm aramid fibres. It was observed from SENB raw data curves that foams with long fibres failed in a progressive manner with fibres arresting the crack progression. In contrast, the control foam failed in a catastrophic manner, as displayed in Fig. 8. The progressive failure of the long fibre specimens does not affect the measured fracture energy; however, it is clearly a benefit for a material in service to fail in such a manner as the total energy absorbed during a complete failure of the foam is increased. Shen and Nutt [15] have also reported fibre bridging in aramid-reinforced sandwich core flexure tests. They noted a significant increase in load after initial failure, again this did not affect the measured property. However, they note the potential for fibre reinforcement to be used to avoid catastrophic failure of

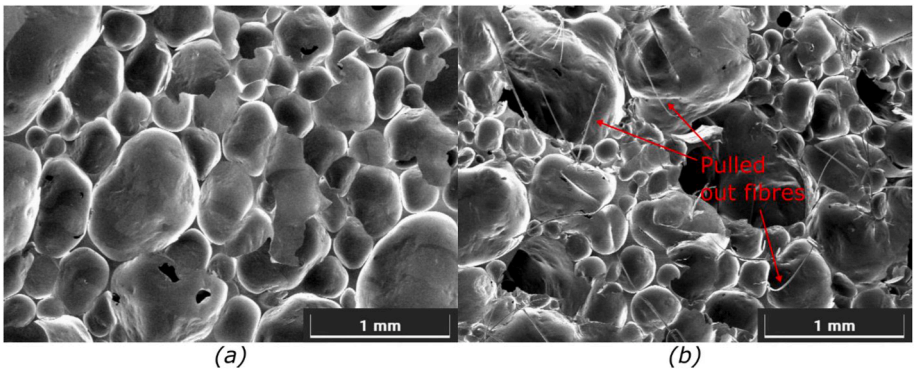

Fig. 9. SEM images of SENB fracture surfaces. (a): Control sample. (b): 6 mm 1 PHR aramid sample showing exposed aramid fibres up to 1 mm in length.

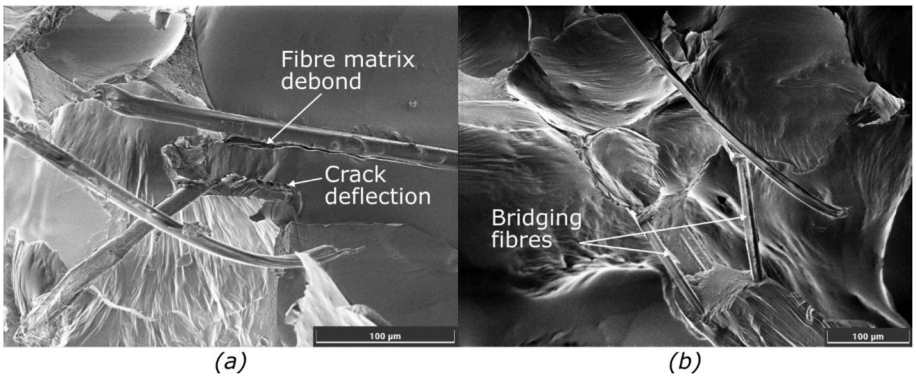

Fig. 10. SENB fracture surfaces 0.75 mm Aramid. (a): Fibres exposed after pull-out and fracture. (b): Fibres exposed after surrounding matrix failure.

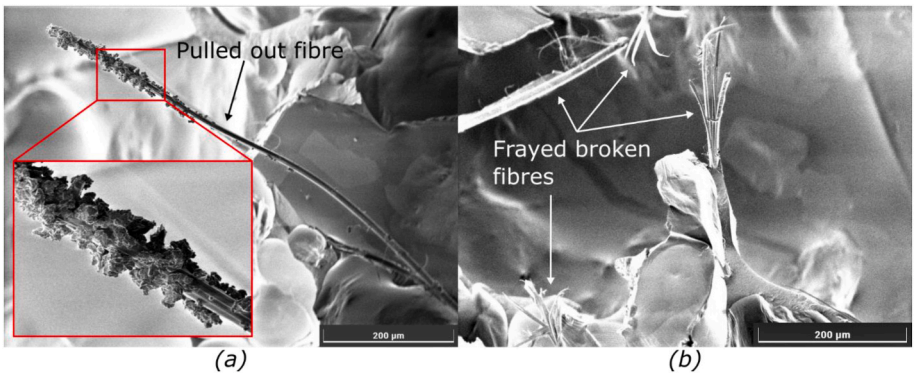

Fig. 11. SENB fracture surfaces 6 mm Aramid. (a): Fibre pulled out with epoxy remaining on the end. (b): Image showing how long aramid fibres fray when broken.

sandwich structures. This is otherwise achieved through increased safety factors leading to an increase in structure weight.

4.5.2. *Fracture morphology: Aramid-Reinforced Foam*

It can be seen in Fig. 9 that the toughening mechanisms of aramid foams include fibre pull-out and fracture as well as crack deflection. The crack direction in all fracture micrographs is from bottom to top. Fig. 9 (a) shows the fracture surface of a control sample. The foam structure is clearly visible and not dissimilar to the polished samples examined in Fig. 2. Moreover, the fracture surface was observed to have no significant deviations from the initial crack plane over the entire crack propagation length. Fig. 9 (b) shows the fracture surface of a foam modified with 1 PHR 6 mm aramid fibres. Significant deviations from the initial crack plane were noted, indicating that the presence of the fibres in the foam caused the crack to deflect. In addition, many exposed fibres can be observed, up to 1 mm long. On the contrary, in the polished sample images, Fig. 2, no exposed fibres were observed. Thus, the visible fibres in Fig. 9 (b) are as a consequence of the fracture process, i.e., they were pulled out of the opposite fracture surface. Fibre pull-out appears to be a principal toughening mechanism within all the aramid fibre-reinforced foams studied here. The fibres shown in Fig. 9 (b) are solitary fibres and appear well dispersed within the foam rather than manifesting as bundles or agglomerates. This represents a key development on fibre-reinforced foams previously reported in the literature where bundles of fibres are mentioned as a manufacturing issue and being less effective at improving mechanical and fracture properties [10,12].

The 0.75 mm aramid fibres caused large increases in the fracture energy of the foam and allowed for a higher fibre loading than longer fibres. Fig. 10 presents examples of fibres on SENB fracture surfaces, Fig. 10 (a) demonstrates that fibres are pulled out but does not show significant amounts of epoxy left on the surfaces of the fibres. It can be seen that the crack is deflected by a fibre as it deviates from its main plane around the base of a pulled-out fibre. Fig. 10 (a) exhibits a case where a microcrack is formed as a fibre debonds from the matrix. In Fig. 10 (b) fibres are seen bridging across where a secondary crack has caused epoxy to fracture off around them. These images clearly demonstrate that the presence of the fibres cause the crack path to deflect and lengthen which require additional energy to propagate [31] and for additional lesser cracks to form leading to an increase in fracture energy.

Fig. 11 (a) shows an image of a pulled-out fibre while (b) shows a series of fractured fibres, the bases of which are situated in nodes and cell walls. It is clear from Fig. 11 (a) that, while the fibre is not completely encased in polymer, there is a significant amount of epoxy in small pieces remaining adhered to the end of the fibre. This contrasts with the clean exposed fibres shown in Fig. 10. The cutting process to prepare the fibres is an aggressive process. It is probable that it affects the sizing of the virgin fibre, especially close to the cutting plane. The shorter 0.75 mm fibres will therefore be more affected by the cutting process than the longer fibres. The broken fibres in Fig. 11 (b) have split and frayed upon fracture. Furthermore, some amount of pull-out has occurred before failure as the fibres are exposed. As the fibres are pulled out, they bridge the crack before failure. Sequential failure of groups of these fibres are responsible for the progressive load-displacement traces, such as the one shown in Fig. 8.

4.5.3. *Fracture energy: carbon-Reinforced Foam*

The experimentally determined fracture energies for all of the manufactured carbon fibre-reinforced foams are given in Table 2. The addition of carbon fibres was found to greatly increase the toughness of the foam from 124 J/m^2 to a maximum of 245 J/m^2. All the carbon fibre-reinforced foams showed an increase in fracture energy over the unmodified foams. However, the link between fibre length and increase in fracture energy is not as clearly defined as with the foams modified with

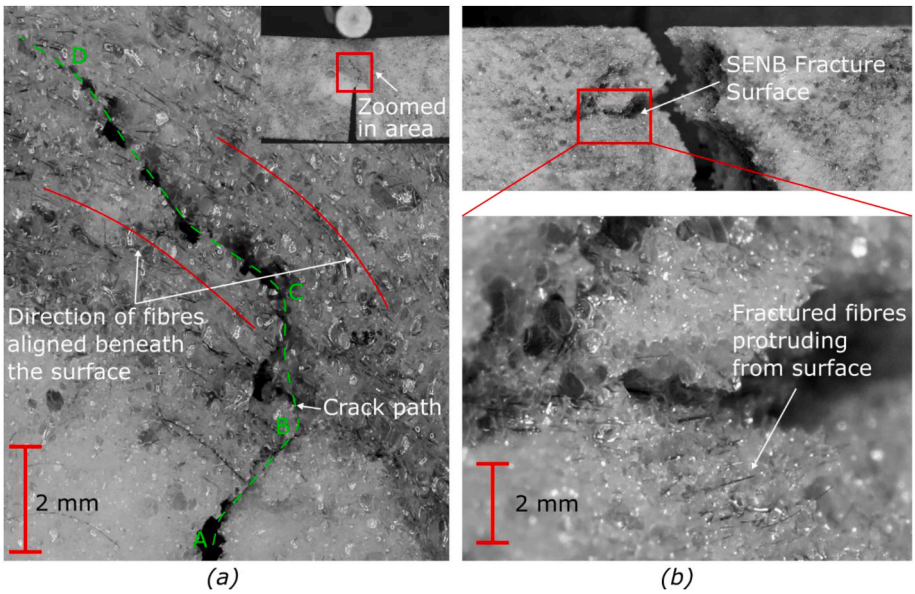

Fig. 12. Photos of 6 mm carbon foam SENB samples. (a): Zoomed in image of the front of a sample during a test. The crack can be seen to initially cross the path of fibres, fracturing them, then deflect to follow a path between aligned fibres within the foam. (b): Fracture surface of a sample showing a crack that has been deflected multiple times and fractured fibres protruding from the fracture surface.

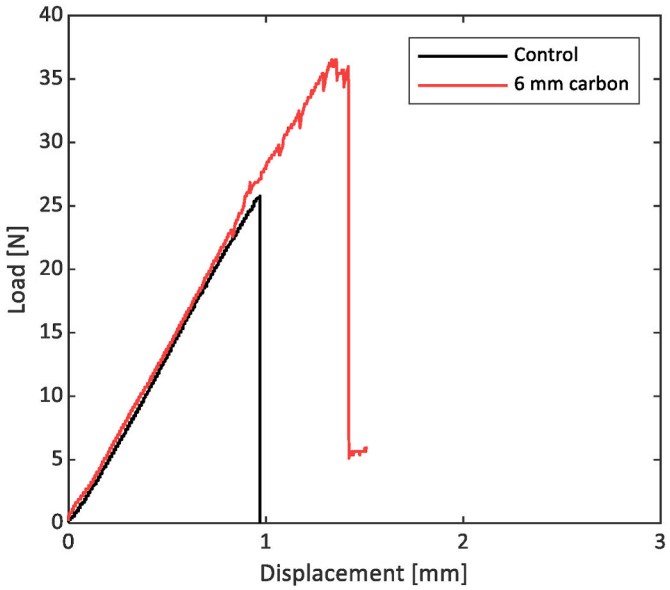

Fig. 13. Load-displacement curves for the SENB testing of carbon 6 mm and control.

aramid fibres.

4.5.4. *Fracture morphology: carbon-Reinforced Foam*

From fractographic analyses conducted on SENB samples, it can be seen that the toughening mechanisms for carbon fibre-reinforced foams also include fibre pull-out and fracture as well as crack deflection. Fig. 12 shows high-fidelity photographs of two 6 mm carbon 1 PHR samples. Fig. 12 (a) shows fibres aligned beneath the surface of the foam of one of the samples. These fibres are 6 mm long and span the whole width of the image. The process of manufacturing the foam involves mixing the resin and fibres together with a rotating blade. During this process, the fibres tend to align tangential to the tip of the mixing blade within the foam mixture. This is especially relevant for longer fibres.

As a result of the circular mixing motion and the subsequent step of pouring the mixture into a separate foaming and casting mould, there is no prevailing global direction for these aligned fibres within the foaming and casting mould. The alignment of fibres is only local. However, since fracture initiation is a local process, this local alignment of fibres is critically important. In Fig. 12 (a), the fracture initially progresses upwards from the initial crack tip from point A to point B, fracturing the fibres in its path. After approximately 2 mm of crack propagation, it straightens to progress mainly upwards to point C before deflecting again to progress upwards to point D, taking a less obstructive path between the aligned fibres within the foam. Fig. 13 plots the raw load versus displacement data for this sample, as the load climbs from 20 to 35 N, small sharp dips in load are clearly visible. During this period of the test, cracking noises were heard, however, periodic imaging revealed no advancement of the main crack during this period. The control foam did not produce these cracking noises; therefore, the noises pre-failure in the fibre reinforced foams are attributable to the failure of the fibres. Based on the analysis of Fig. 12 (a), Fig. 13, the periodic imaging of the test, and the noises heard, the fibres fail before the crack advances. The failure strain of the carbon fibres is lower than that of the epoxy. As a result, when the sample is loaded and the area ahead of the crack is strained past the fibre failure strain, the fibres fail sequentially. When the epoxy failure strain is reached the broken fibres provide a path for the crack to travel through until intact fibres prevent further propagation in that direction. The crack then deflects along the aligned fibres and the sample fails suddenly. This deviation from the main plane of the crack will give rise to mode II contributions and a resultant increase in fracture energy. The crack path in this sample is also longer than an unreinforced sample, again causing an increase in fracture energy.

The toughening mechanisms taking place within this sample depended greatly upon the state of fibre-reinforcement ahead of the crack tip, in this instance the arrangement of the fibres was conducive to a high fracture energy. Some samples did not have fibres positioned in such a way as to give as high a fracture energy. This fact explains the larger standard deviations in Tables 1 and 2 for the fracture data of long fibre foams. Fig. 12 (b) shows the fracture surface of a different sample, it is clear from the upper image that the crack path has been deflected. The lower image shows broken fibres protruding from the surface, the fibres appear to be individual and well dispersed. From these images it is clear that fibre breakage is a key toughening mechanism. Similar photographs are not shown for aramid foams as the yellow fibres are

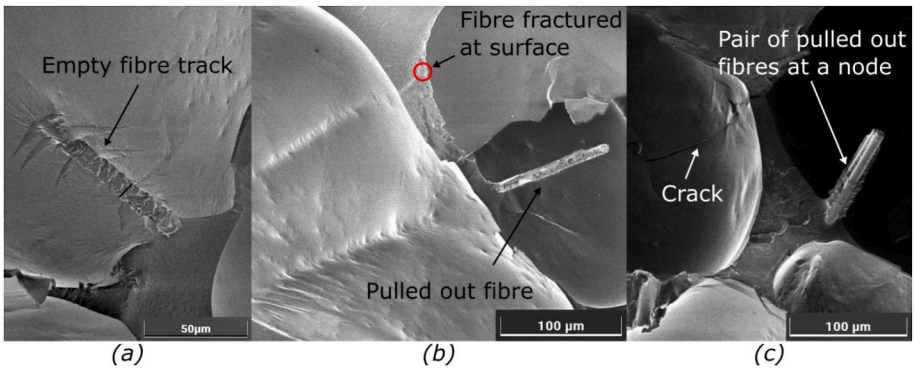

Fig. 14. SENB fracture surfaces of carbon foams. (a): Empty fibre track from a 3 mm fibre. (b) Example of both a pulled out and fractured 3 mm fibre. (c): Example of two 6 mm fibres pulled out.

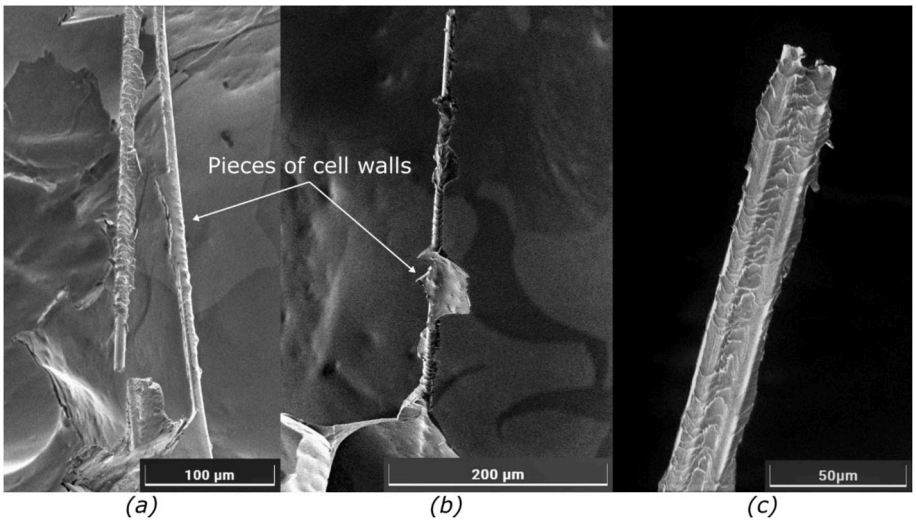

Fig. 15. SENB fracture surfaces of carbon foam. (a) 3 mm fibres bridging after epoxy has fractured off. (b): 1.5 mm fibre pulled out with epoxy remaining. (c): Pair of 6 mm fibres pulled out coated with epoxy.

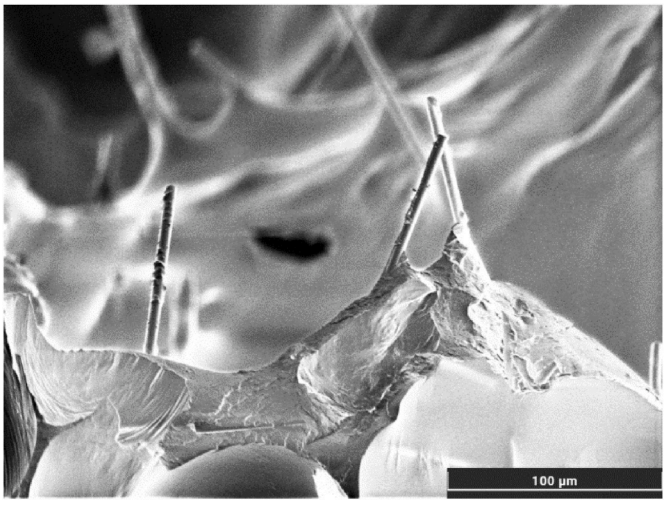

Fig. 16. SEM image of a SENB fracture surface showing milled carbon fibres pulled out. Note the relatively clean surfaces of the milled fibres.

difficult to distinguish.

The toughening mechanisms in carbon fibre-reinforced foams are highlighted in Fig. 14. Fig. 14 (a) shows an empty fibre track, from wher7e a fibre has been pulled during the fracture event. The fibre was encased in epoxy, this is evident as the track is 2 μm wider than the 8-μm diameter fibres. The rough surface of the fibre track reinforces this, a smooth track would indicate that the fibre was not well adhered. Fig. 14 (b) demonstrates an example of how fibres can lie within a cell wall. One fibre is fractured at the crack plane while the second fibre has been pulled-out and is mostly encased in epoxy. Fig. 14 (c) exhibits a pair of fibres lying within a node that have been pulled out and are also both encased in epoxy. Fig. 15 (a) and (b) show long exposed fibres with significant parts of cell walls remaining after fracture. The extra fracture surfaces created by these fibres, and the associated energy absorption, represents a significant toughening mechanism. The main toughening from fibre pull-out is from the shear at the interface due to interfacial fictional sliding [32]. Fig. 15 (c) shows a pair of fibres pulled out encased in epoxy showing clear signs of epoxy shear failure on the surface. While the aramid fibres were found by themselves, it was not uncommon to find longer carbon fibres in pairs such as in Fig. 14 (c) and Fig. 15 (a) and (c). Furthermore, while aramid fibres frayed and split when broken, carbon fibres exhibited clean fractures.

Fig. 16 shows a series of milled fibres protruding from the fracture surface. A key difference between these fibres and the longer, chopped carbon fibres discussed earlier is the lack of epoxy polymer adhering to the fibre. The chopped fibres were originally sized for use with epoxy as the matrix and so are encased in epoxy when pulled out, whereas the milled fibres did not have any appropriate sizing and so pull out with a very clean surface, almost devoid of polymer. Despite this, the milled

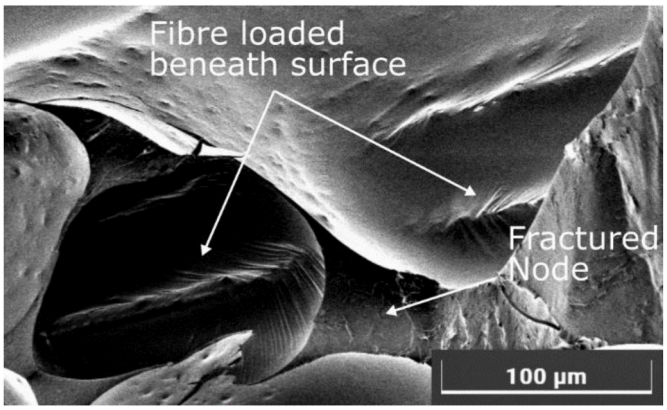

Fig. 17. SEM image of a 6 mm fibre below the surface of a fractured node having been loaded.

fibres provide benefit as the pull-out of clean fibres still absorbs energy through interfacial frictional sliding [32].

Fig. 17 shows a carbon fibre below the surface of a fractured node from an SENB sample. From the striations leading to the cell wall and node, it is clear that the fibre and the surrounding polymer material was loaded as the crack passed along the main fracture plane, providing a stiffening effect. It is interesting to note that the fibres within the foam causing this stiffening effect and increasing constraint may well be reducing the fracture energy if they are not within the crack path triggering energy absorption mechanisms.

4.6. Effect on face-core interface

Once the improvements in fracture performance of fibre-reinforced foams had been confirmed, a set of SCB face-core debond tests were carried out on both a control foam and a 2.5 PHR 0.75 mm aramid foam. The results of this SCB testing can be found in Table 3. An example of a load versus displacement for each type of sample is shown in Fig. 18. Adding 0.75 mm 2.5 PHR aramid fibres to the foam core of a sandwich structure increases face-core propagation fracture toughness by 50% and initiation fracture toughness by 30%. Fig. 19 shows images taken of the side of both types of SCB samples during testing, the images show that foam is fractured off the core and remains on the face-sheet surface. As a result, similar toughening mechanisms observed in SENB foam fracture have caused the increase in toughness of this interface. These mechanisms are clear in face-sheet -side fracture surface images in Fig. 20 (a) and (b), exposed fibres that have been pulled out are clear in both photographs and SEM images. There is an increase in the difference between the propagation and initiation fracture toughness with the addition of aramid fibres. This increase suggests an increase in the R-curve behaviour. This is due to material, mainly the fibres, bridging the gap behind the crack tip. As the aramid foam fractures, the fibres are often pulled out as seen in the side-on image in Fig. 19, and both the SEM micrograph and microscope image of the fracture surfaces in Fig. 20. Therefore, the fibres are being pulled out of the foam behind the crack tip, causing an increase in R-curve behaviour and a large increase in the difference between propagation and initiation fracture toughness.

To further demonstrate the role of fibre bridging on improving the toughness of the face-core interface, a side-on micrograph was taken using SEM of the surface of an 'as-machined' foam. This is shown in Fig. 21. Exposed fibres on the surface can be clearly observed. This is the surface that the face-sheet will ultimately be infused on. The aramid fibres are much tougher and difficult to machine than the relatively friable polymer foam structure. As a result, during the machining process, they tend to deflect under the cutting blade and bounce back once the blade has passed. Fibres exposed during foam machining leave an ideal surface for the face-sheet matrix resin to bond to. Control foam samples showed failure partially within the foam. It was hypothesised that were the foam made tougher, the failure of the SCB specimens would be mostly interfacial and the foam would be left intact. However, it is clear from the results presented here, that in adding fibres to the foam the interfacial bond itself has also been improved due to the exposed fibres on the surface.

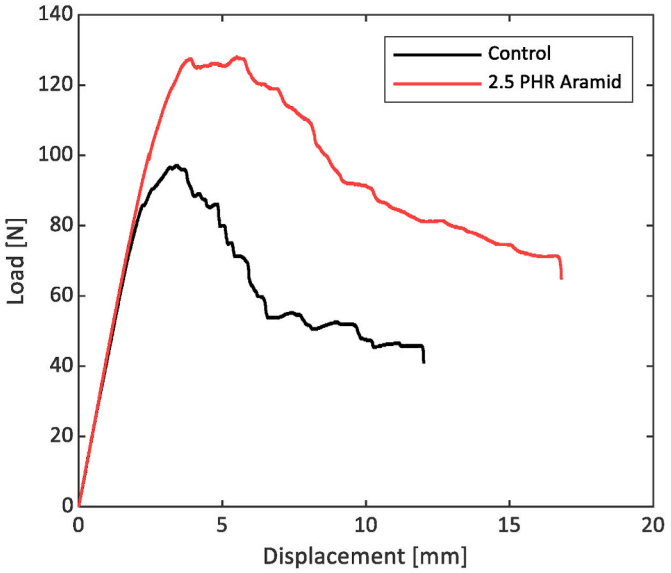

Fig. 18. Load-displacement curves for the SCB testing of a control and a 2.5 PHR 0.75 mm aramid sample.

5. Conclusion

Low density short carbon and aramid fibre-reinforced epoxy foams have been successfully synthesised for the first time. Improvements in the fracture performance of epoxy foams have been achieved through the addition of these fibres. The effect of fibre type, length and loading have been investigated. The incorporation of 5 PHR 0.75 mm aramid led to a maximum increase in fracture energy of 107% from 124 J/m^2 to 256 J/m^2. The main toughening mechanisms observed were fibre pull-out, fibre fracture and crack deflection and arrest. The addition of 2.5 PHR 0.75 mm aramid fibre and 0.6 mm carbon fibre both cause an increase in compressive yield strength of ~10%, further additions cause a drop in strength. The addition of aramid fibre causes an increase in foam density of up to 16%, short carbon fibres only increased density up to 5% while 3 and 6 mm carbon fibres reduced density by up to 2%. When used in a composite sandwich structure, 0.75 mm 2.5 PHR aramid fibre-reinforced foam improves face-core initiation and propagation fracture toughness by 30 and 50% respectively. This investigation has shown that fibre reinforced epoxy foams can outperform their unreinforced

Table 3
SCB results for aramid 0.75 mm 2.5 PHR foam and control foam.

Fibre Length [mm]	Fibre Loading [PHR]	*Initiation* G_c [J/m^2]	% change	*Propagation* G_c [J/m^2]	% change	*Prop – Init* G_c [J/m^2]	% change
–	–	231 ± 43	–	277 ± 38	–	46 ± 7	–
0.75	2.5	301 ± 52	+30	416 ± 24	+50	115 ± 54	+150

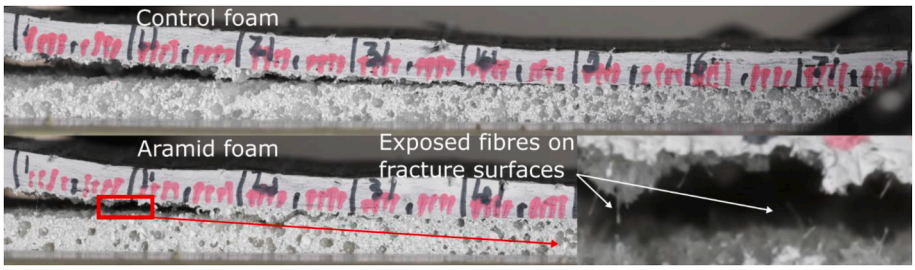

Fig. 19. Side view of SCB tests showing exposed fibres in the aramid foam sample.

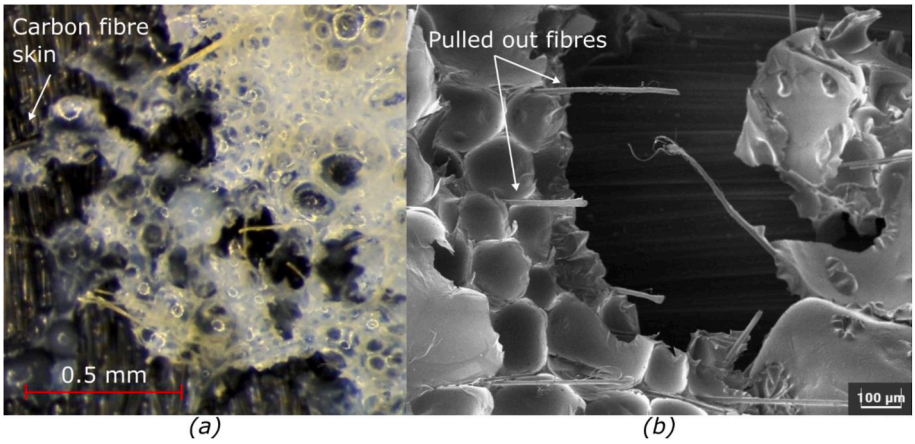

Fig. 20. SCB face-sheet side fracture surface. (a) Digital photograph. (b) SEM image.

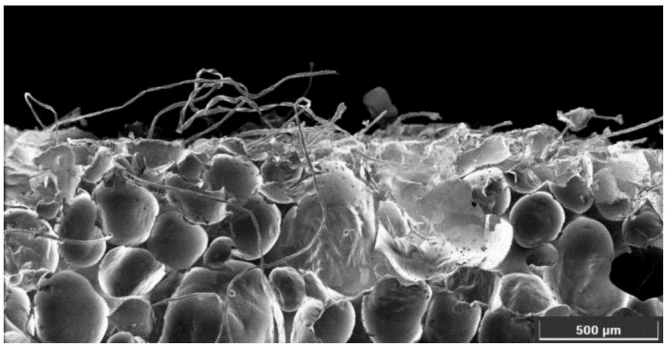

Fig. 21. SEM image showing the edge of a machined sample of aramid foam showing exposed fibres on the surface.

counterparts with few drawbacks other than a slight increase in density and increased manufacturing complexity. There are more gains to be realised if longer fibres can be used to manufacture low density foams without large voids which reduce compressive strength. Large voids will also cause increased resin uptake during a resin infusion or require more adhesive during bonded sandwich structure manufacture. For this reason, the most attractive option is to make use of short carbon and aramid fibres in epoxy foams.

Author statement

George Irven: Conceptualization, Methodology, Investigation, Formal analysis, Writing – Original Draft, Writing – Review and Editing, Declan Carolan: Conceptualization, Conceptualization, Methodology, Formal Analysis, Writing – Review and Editing, Supervision, Alexander Fergusson: Writing – Review and Editing, Supervision, Resources, Funding Acquisition, John P. Dear: Writing – Review and Editing, Supervision, Funding Acquisition.

Declaration of competing interest

The authors declare that they have no known competing financial interests or personal relationships that could have appeared to influence the work reported in this paper.

Data availability

Data will be made available on request.

Acknowledgements

George Irven would like to acknowledge an EPSRC faculty CASE PhD studentship with FAC Technology. Grant number [EP/R513052/1].

Declan Carolan acknowledges the support of UKRI, Future Leaders Fellowship. Grant number [MR/T023406/1].

References

[1] Gibson LJ, Ashby MF. Cellular solids. Cambridge University Press; 1997.
[2] Rolfe E, Kaboglu C, Quinn R, Hooper PA, Arora H, Dear JP. High velocity impact and blast loading of composite sandwich panels with novel carbon and glass construction. J Dyn Behav Mater 2018;4:359–72. https://doi.org/10.1007/s40870-018-0163-5.
[3] Irven G, Duncan A, Whitehouse A, Carolan D, Fergusson AD, Dear JP. Impact response of composite sandwich structures with toughened matrices. Mater Des 2021;203:109629. https://doi.org/10.1016/j.matdes.2021.109629.
[4] Marşavina L. Fracture mechanics of cellular solids. In: CISM int Cent Mech Sci Courses lect, 521. Vienna: Springer; 2010. p. 1–46. https://doi.org/10.1007/978-3-7091-0297-8_1.
[5] Marşavina L, Linul E. Fracture toughness of rigid polymeric foams: a review. Fatig Fract Eng Mater Struct 2020;43:2483–514. https://doi.org/10.1111/ffe.13327.
[6] Song W, Konstantellos G, Li D, Lee KY. Short carbon fibre-reinforced epoxy foams with isotropic cellular structure and anisotropic mechanical response produced

from liquid foam templates. Compos Sci Technol 2019;184. https://doi.org/10.1016/j.compscitech.2019.107871.
[7] Alonso MV, Auad ML, Nutt SR. Short-fiber-reinforced epoxy foams. Compos Part A Appl Sci Manuf 2006;37:1952–60. https://doi.org/10.1016/j.compositesa.2005.12.011.
[8] Alonso MV, Auad ML, Nutt SR. Modeling the compressive properties of glass fiber reinforced epoxy foam using the analysis of variance approach. Compos Sci Technol 2006;66:2126–34. https://doi.org/10.1016/j.compscitech.2005.12.016.
[9] Cotgreave TC, Shortall JB. Failure mechanisms in fibre reinforced rigid polyurethane foam. J Cell Plast 1977;13:240–4. https://doi.org/10.1177/0021955X7701300401.
[10] Cotgreave TC, Shortall JB. The mechanism of reinforcement of polyurethane foam by high-modulus chopped fibres. J Mater Sci 1977;12:708–17. https://doi.org/10.1007/BF00548161.
[11] Cotgreave TC, Shortall JB. The fracture toughness of reinforced polyurethane foam. J Mater Sci 1978;13:722–30. https://doi.org/10.1007/BF00570506.
[12] Carling MJ. Fracture mechanics of short fibre composites. Imperial College London; 1988.
[13] Desai AA, Nutt SR, Alonso MV. Modeling of hybrid composite foams. J Cell Plast 2010;46:113–28. https://doi.org/10.1177/0021955X09351195.
[14] Desai AA, Auad ML, Hongbin Shen H, Nutt SR. Mechanical behavior of hybrid composite phenolic foam. J Cell Plast 2008;44:15–36. https://doi.org/10.1177/0021955X07078021.
[15] Shen H, Nutt SR. Mechanical characterization of short fiber reinforced phenolic foam. Compos Part A Appl Sci Manuf 2003;34:899–906. https://doi.org/10.1016/S1359-835X(03)00136-2.
[16] Shen H, Lavoie AJ, Nutt SR. Enhanced peel resistance of fiber reinforced phenolic foams. Compos Part A Appl Sci Manuf 2003;34:941–8. https://doi.org/10.1016/S1359-835X(03)00210-0.
[17] Viana GM, Carlsson LA. Influences of foam density and core thickness on debond toughness of sandwich specimens with PVC foam core. J Sandw Struct Mater 2016;5:103–18. https://doi.org/10.1177/1099636203005002020.
[18] ASTM D5045-14. Standard test methods for plane-strain fracture toughness and strain energy release rate of plastic materials. West Conshohocken, USA: American Society for Testing and Materials; 2014. https://doi.org/10.1520/D5045-14. n.d.
[19] Viana GM, Carlsson LA. Mechanical properties and fracture characterization of cross-linked PVC foams. J Sandw Struct Mater 2002;4:99–113. https://doi.org/10.1177/1099636202004002227.
[20] Pugna A, Negrea R, Linul E, Marşavina L. Is fracture toughness of pur foams a material property? Stat . Materials Mater (Basel) 2020;13:1–13. https://doi.org/10.3390/ma13214868.
[21] Zenkert D, Bäcklund J. PVC sandwich core materials: mode I fracture toughness. Compos Sci Technol 1989;34:225–42. https://doi.org/10.1016/0266-3538(89)90030-4.
[22] Saenz EE, Carlsson LA, Karlsson AM. In situ analysis of fatigue crack propagation in polymer foams. Eng Fract Mech 2013;101:23–32. https://doi.org/10.1016/j.engfracmech.2012.10.009.
[23] ASTM D1621-16. Standard test method for compressive properties of rigid cellular plastics. West Conshohocken, USA: American Society for Testing and Materials; 2016. https://doi.org/10.1520/D1621-10.2. n.d.
[24] Ratcliffe JG. Sizing a single cantilever beam specimen for characterizing facesheet-core debonding in sandwich structure. 2010. https://doi.org/10.1177/0021998311401116.
[25] Ratcliffe JG, Reeder JR. Sizing a single cantilever beam specimen for characterizing facesheet-core debonding in sandwich structure. J Compos Mater 2011;45:2669–84. https://doi.org/10.1177/0021998311401116.
[26] Glaessgen EH, Reeder JR, Sleight DW, Wang JT, Raju IS, Harris CE. Debonding failure of sandwich-composite cryogenic fuel tank with internal core pressure. J Spacecraft Rockets 2005;42:613–27. https://doi.org/10.2514/1.5567.
[27] Adams D, Nelson J, Bluth Z, Hansen C. Development and evaluation of fracture mechanics test methods for sandwich composites. Baltimore: FAA JAMS Tech. Rev. Meet.; 2012.
[28] Adams D, Nelson J, Bluth Z. Development and evaluation of fracture mechanics test methods for sandwich composites. FAA Technical Review: https://pdfs.semanticscholar.org/bd21/65b6c116ba8c3c818907d34c0f57351da09a.pdf; 2011.
[29] Suo Z, Hutchinson JW. Sandwich test specimens for measuring interface crack toughness. Mater Sci Eng, A 1989;107:135–43. https://doi.org/10.1016/0921-5093(89)90382-1.
[30] Rajput MS, Burman M. K\"{o}ll J, Hallstr\"{o}m S. Compression of structural foam materials – experimental and numerical assessment of test procedure and specimen size effects. J Sandw Struct Mater 2019;21:260–88. https://doi.org/10.1177/1099636217690500.
[31] Faber KT, Evans AG. Crack deflection processes-II. Experiment. Acta Metall 1983;31:577–84. https://doi.org/10.1016/0001-6160(83)90047-0.
[32] Hull D, Clyne TW. An introduction to composite materials. Cambridge University Press; 1996. https://doi.org/10.1017/cbo9781139170130.